Modeling of gas dynamics for a laser-generated plasma: Propagation into low-pressure gases

H. C. Le, D. E. Zeitoun, and J. D. Parisse

*IUSTI-CNRS UMR 6595, Université de Provence–Technopôle de Château Gombert, 5 rue Enrico Fermi,
13453 Marseille Cedex 13, France*

M. Sentis,[1] and W. Marine[2]

[1]*IRPHE-CNRS UMR 6594, Faculté des Sciences de Luminy, Case 918, 13288 Marseille Cedex 09, France*
[2]*GPEC-CNRS UMR 6631, Faculté des Sciences de Luminy, Case 918, 13288 Marseille Cedex 09, France*

The physical phenomena involved during three-dimensional axisymmetric laser-induced plasma expansion into background gas are numerically studied. For this purpose, a multispecies hydrodynamic model is developed which considers the effects of mass and ambipolar diffusions, thermal conduction, viscosity, and nonequilibrium conditions for ionization. This model is applied to describe quantitatively the Si plasma plume expansion into Ar or He gases. It is shown that the mechanism of plasma expansion depends critically on both the pressure and mass of the background gas. The shock front expansion is found to be strongly correlated with ion dynamics. A pronounced difference between heavy-particle and electron temperatures indicates a persistent lack of equilibrium between the heavy particle and the electron in the plasma plume expansion. The Si atoms of the rarefied plume are essentially driven by the backward-moving background gas as a result of a mass diffusion process. It is also noted that the diffusion processes are only important in the last expansion stage, and are less significant in the first stage. Therefore, it is shown that a computation which does not include diffusion effects (Euler equations) can adequately describe only the earliest stage of plasma expansion into background gas. The ability of the Navier-Stokes hydrodynamic multispecies model to predict the key role of the background gas type (Ar, He) and pressure is demonstrated.

PACS number(s): 52.50.Jm, 52.65.−y

I. INTRODUCTION

Pulsed laser deposition (PLD) has become a flexible and effective method of depositing a wide variety of thin films extending from high-T_c superconductors to dielectric materials [1]. More recently, PLD was shown to be a technologically attractive technique for producing silicon nanostructures [2]. Physical processes during PLD produced by short laser pulses (ranging from picoseconds to nanoseconds) and relatively low laser fluences (<10 J/cm^2) can be described by four successive stages [3,4]: (i) evaporation of the target material; (ii) interaction of the evaporated cloud with the laser beam, resulting in cloud heating and plasma formation; (iii) plasma plume expansion into the vacuum or background gas environment; and (iv) deposition of material on a substrate. The first two processes occur during the laser pulse. For nanosecond laser pulses, it may be assumed that the third process (i.e., the expansion stage) starts after the laser pulse has terminated, and thus can be considered separately. The first two processes have been widely discussed elsewhere [3–5].

Plasma expansion into a vacuum environment is a simple adiabatic regime which can be fully predicted by theoretical models and numerical gas dynamic simulations [3,4]. The plasma behavior into a background gas becomes considerably more complicated due to the rise of new physical processes involved such as deceleration, shock wave formation, thermal conduction, diffusion, recombination, and clustering. Previously a deeper understanding of the plasma plume expansion was gained by combining experimental results with models derived from numerical simulations [1,6,7]. For low

gas pressure (less than $\sim$100 mTorr), plasma expansion was described by Monte Carlo simulation [8], whereas for higher pressure many numerical simulations were performed using compressible and nondissipative conservation equations for mass, momentum, and energy (i.e., Euler equations) [7,8,10]. The latter hydrodynamic approach is advantageous for providing density, velocity, and temperature profiles across the plasma plume as a function of time, and leading to quantities which may be compared with experimental measurements [7,8,10]. However for Euler modeling, all the simulated species, including neutral atoms and ions, have the same velocity (i.e., fluid velocity), whereas experimental results indicate that neutral atoms are characterized by a lower most probable velocity in comparison with ionized atom velocities [3,11–13]. In fact, owing to the presence of large electron density gradients in the compression shock, and to the high mobility of electrons, conditions are favorable for the diffusion of electron gas with respect to ion gas, and to the creation of space charges. Together with viscosity and heat conduction, diffusion affects the structure of the shock front and thus the thermalization of plume species [14]. Finally, during plasma expansion into the background gas, a considerable part of the ionization energy is converted into hydrodynamic flow via recombination processes [9,14]. Thus the plasma plume expansion should not be considered in ionization equilibrium.

In the present work, a multispecies three-dimensional axisymmetric model is developed to describe laser-induced plasma expansion into background gases. The full Navier-Stokes computation with mass and forced diffusions, thermal conduction, and viscosity is used for the first time, to our

knowledge, to improve the predictive capability of the computer simulation. The model also incorporates the nonequilibrium condition for ionization and recombination. The study is focused on a presentation of the physical and numerical modeling (Navier-Stokes equations, transport properties, ionization, and recombination mechanisms), and on a quantitative description of the spatial and temporal evolution of the laser-induced Si plasma plume into both Ar and He gases. Modeling conditions are characterized by several laser-ablation processing parameters including energy densities, background gas nature, and pressure. Differences between Navier-Stokes and Euler computations are outlined. Finally, the plasma expansion behavior into the background gas, and some interesting physical features such as the temperature evolution of atoms and electrons, the shock front and ion dynamics, and ionization degree variations are presented and discussed.

II. PHYSICAL AND NUMERICAL MODELING

A. Physical consideration

The gas dynamics processes are studied in the case of irradiation of a pure silicon target, placed in a background gas, with an excimer laser beam (ArF, $\lambda = 193$ nm). The laser fluence range is 1.5–2.4 J/cm^2, providing a good supply of singly ionized Si while avoiding higher ionization states [2,12,13]. Four species are considered in the hydrodynamic model: Si I (neutral atom, $i=1$), Si II (singly ionized atom, $i=2$), electrons ($i=3$) and Ar I or He (neutral atom, $i=4$). The background gas of Ar or He is assumed to be neutral because of its high ionization energy (16 and 24 eV, respectively). The plasma plume and background gas are treated as a compressible flow [3,8]. The plasma is assumed to be quasineutral, and two-temperature modeling (T, T_e) is used to describe the ionization nonequilibrium condition [9,14]. The electron temperature T_e deviates from the heavy-particle temperature T because of the slow rate of energy transfer between electrons and heavy particles caused by the large mass disparity between the electrons and heavy particles.

B. Governing flow equations

The three-dimensional axisymmetric compressible Navier-Stokes equations are solved for a multispecies gas, including the effects of mass and forced diffusion and thermal conduction and viscosity, and are written as follows [15]:

$$\frac{\partial \rho_i}{\partial t} + \text{div}[\rho_i(\vec{v} + \vec{v}_{di})] = \omega_i, \quad i=1,...4, \tag{1}$$

$$\frac{\partial \rho \vec{v}}{\partial t} + \text{div}(\rho \vec{v}\vec{v} - P\bar{\bar{I}} + \bar{\bar{\tau}}) = 0, \tag{2}$$

$$\frac{\partial E_a}{\partial t} + \text{div}[E_a \vec{v} - (-P_a \bar{\bar{I}} + \bar{\bar{\tau}})\vec{v} + \vec{q}] = S_a, \tag{3}$$

$$\frac{\partial E_e}{\partial t} + \text{div}[E_e + P_e)(\vec{v} + \vec{v}_{die})] = S_e + F_e. \tag{4}$$

In these equations, ρ_i, $\vec{v}_{di}$, and ω_i are the density, the diffusion velocity, and mass source term of species i, respectively. $\vec{v}$ is the velocity, ρ is the density of the mixture, P_a and P_e are the atom-ion and electron pressure, respectively, P is the overall pressure, and $\bar{\bar{\tau}}$ is the viscous shear stress tensor. E_a and E_e are the atom-ion and electron energies, and S_a and S_e are the atom-ion and electron energy source terms.

An ideal-gas equation of state is assumed for each species (heavy particle, electron). The overall pressure P is given by

$$P = P_a + P_b = \sum_{i \neq e} \rho_i \frac{RT}{\hat{M}_i} + \rho_e \frac{RT_e}{\hat{M}_e}, \tag{5}$$

where $\hat{M}_i$ is the molecular weight of species i, $\hat{M}_e$ is the molecular weight of the electron, and R denotes the universal gas constant.

The heat conductive flux $\vec{q}$ can be expressed as

$$\vec{q} = -\lambda_m \vec{\nabla} T + \sum_i \vec{v}_{d_i} \rho_i h_i, \tag{6}$$

where λ_m is the gas mixture's thermal conductivity. The specific enthalpy h_i can be written as

$$h_i = \int_0^T C_{p_i} dT + h_i^0, \tag{7}$$

where C_{p_i} and h_{i_a} are the specific heat at constant pressure and the heat of the formation of species i, respectively.

The rigorous form of diffusion velocity given by Curtiss and Hirschfelder [16] is usually difficult to include in numerical simulation. Therefore, a simplification of the expression for diffusion velocity is necessary. Oran and Boris give useful formulas for evaluating the diffusion velocity and transport coefficients [15]. The diffusion velocities are solutions to the system of equations [15]

$$\text{grad } X_i = \sum_j \frac{X_i Y_j}{D_{ij}} (\vec{v}_{dj} - \vec{v}_{di}), \tag{8}$$

where, for each species i, X_i is the mole fraction, Y_i is the mass fraction, and D_{ij} is the diffusivity of the species i into the species j. Here the contributions of thermal and pressure diffusions, which are generally small in comparison with the mass diffusion, are neglected.

Forced diffusion due to the presence of an electric field also has to be considered. Electrons possess higher mobility and diffuse faster than ions, leaving behind them an excess of positive charges. The electric field produced by this initial charge separation tends toward a slowing down of the electrons and an acceleration of the ions. Thus the electric field affects the diffusion processes of the electrons and ions. The electric force also acts on the charged particles and may significantly change their energy. The rigorous treatment of the problem of forced diffusion by an electric field requires a complex system of equations [17]. Therefore, here we tend to consider this effect approximately by introducing the ambipolar diffusion concept (i.e., a small degree of charge separation) for charged particles (ionized atom and electron) [17]. Ambipolar diffusion occurs when an electron pressure gradi-

ent exists in an ionized gas, but when there is not a great charge separation [17]. For low laser fluences, near the plasma ignition threshold, a small degree of charge separation may be assumed. Because of the linking of the electron and ion diffusion by the electric field, an ambipolar diffusion coefficient is twice the value of an ionic diffusion coefficient [17]. The electric field term F_e, which appears in Eq. (4), is given by [14,17].

$$F_e = (\vec{v} + \vec{v}_{die}) \cdot \text{grad } P_e. \quad (9)$$

For the thermal conductivity of the mixture [18], an extremely useful equation was given by Mason and Saxena [18], and reported by Oran and Boris [15],

$$\lambda_m = \sum_i \lambda_i \left[1 + \frac{1.065}{2\sqrt{2}n_i} \sum_{k \neq i} n_k \Phi_{ik} \right]^{-1}, \quad (10)$$

where n_k is the density of species k; Φ_{ik} is given by

$$\Phi_{ik} = \frac{[1 + (\lambda_i/\lambda_k)^{1/2}(\hat{M}_i/\hat{M}_k)^{1/4}]^2}{[1 + \hat{M}_i/\hat{M}_k]^{1/2}}; \quad (11)$$

and λ_i is the thermal conductivity of species i.

The viscosity of a gas mixture was given by Wilke [19],

$$\mu_m = \sum_i \mu_i \left[1 + \frac{\sqrt{2}}{4n_i} \sum_{k \neq i} n_k \varphi_{ik} \right]^{-1}, \quad (12)$$

where μ_i is the viscosity of the species i, n_i and n_k are the densities of the species i and k, respectively, and φ_{ik} is expressed as

$$\varphi_{ik} = \frac{[1 + (\mu_i/\mu_k)^{1/2}(\hat{M}_k/\hat{M}_i)^{1/4}]^2}{[1 + \hat{M}_k/\hat{M}_i]^{1/2}}. \quad (13)$$

A detailed description of the transport coefficients (thermal conductivity and viscosity of the individual Si, Ar, and He gases, binary diffusion), which are expressed as polynomial functions of the temperature, can be found in Ref. [20].

C. Nonequilibrium ionization model

The source terms in Eqs. (2), (4), and (5) depend on the ionization and recombination rate constants which were given by Zeldovich and Raizer [14], and were discussed in detail in Ref. [9]. The photoabsorption process is neglected because for such ablation conditions the plasma plume is a nonabsorbant medium [9]. The following processes are considered to estimate the rate constants: (a) ionization of ground state Si I and three-body recombination into the ground state,

$$\text{Si I} + e + 8.1 \text{ eV} \leftrightarrow \text{Si II} + e + e; \quad (14)$$
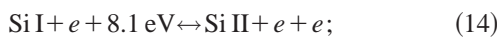
and (b) photorecombination into the ground state,

$$\text{Si II} + e \rightarrow \text{Si I} + h\nu. \quad (15)$$

The electron impact ionization rate k_{fa} is expressed as

$$k_{fa} = 2 \frac{(2\pi m_e k T_e)^{3/2}}{n_e h^3} k_{ba} \exp\left(\frac{-U_i}{T_e}\right), \quad (16)$$

where m_e is the mass of the electron, n_e is the electronic density, U_i is the ionization potential of the atom in the ground state, and k is the Boltzmann constant. C_2 is the three-body recombination rate constant given by

$$k_{ba} = \frac{4\pi(2\pi)^{1/2}}{9} \frac{e^{10}}{m_e^{1/2}(kT_e)^{9/2}} n_e, \quad (17)$$

where e is the charge of the electron. The photorecombination rate C_3 is

$$k_{fb} = 2 \times 10^{-13}/\sqrt{T_e}, \quad (18)$$

where T_e is in eV.

So the source terms of mass ω_i in Eqs. (1) are

$$\omega_1 = m_1 n_e [(C_3 + C_2)n_2 - C_1 n_1], \quad (19)$$

$$\omega_2 = m_2 n_e [-(C_3 + C_2)n_2 + C_1 n_1], \quad (20)$$

$$\omega_3 = \omega_2(m_3//m_2), \quad (21)$$

$$\omega_4 = 0, \quad (22)$$

where n_1 is the neutral atom density, n_2 is the ionized atom density, and m_i, is the mass of one atom of the species i. m_i is given by the formula $m_i = \hat{M}_i/N_A$, where N_A is the Avogadro number.

The source term of energy S_a in Eq. (3), obtained by neutral atom and ion elastic collision exchange with electrons, can be written [16]

$$S_a = 3R\rho_e(T_e - T)\left(\frac{SRT_e}{\pi\hat{M}_e}\right)^{1/2} \sum_{i \neq e} \frac{\rho_e n_i}{\hat{M}_e^2} \sigma_{ei}, \quad (23)$$

where $\hat{M}_e$ and $\hat{M}_i$ are the molecular weight of the electron and species i, respectively. σ_{ei} is the cross section for electron-species i interaction [21].

The source term of energy S_e in Eq. (4), gained and lost by electrons in elastic and nonelastic collisions, is given by [9,14]

$$S_e = -S_a + \frac{2}{3}(E^* n_2 k_{ba} - U_i n_1 k_{fa} - \frac{3}{2}kT_e k_{fb}), \quad (24)$$

where E^* is the energy gained by the electron during a three body recombination reaction, and can be expressed as a function of electron density and temperature [9,14].

D. Numerical integration

In order to describe the unsteady plasma evolution, the Navier-Stokes equations (1)–(5) are numerically solved with the flux corrected transport algorithm LCPFCT [17,22] for the convective terms of these equations. This approach is coupled with a second-order finite volume method for integrating the viscous terms [23]. It is noted that the LCPFCT is a nonlinear monotone algorithm that is fourth order accurate in phase. The integration is carried out by a two-step predictor-corrector procedure with diffusive and antidiffu-
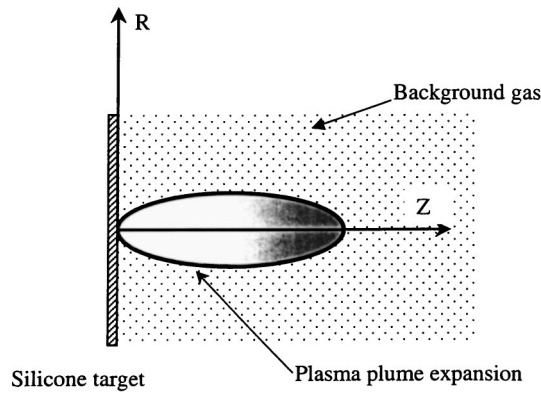
FIG. 1. Schematic diagram of the laser-induced plasma plume expansion.

sive steps successively. The first step modifies the linear properties of a high-order algorithm by adding diffusion during convective transport to prevent dispersive ripples from arising. The added diffusion is removed in an antidiffusion step. The calculations maintain high-order accuracy without requiring artificial viscosity to stabilize them. A detailed discussion of these numerical properties of the LCPFCT method can be found in Ref. [22].

It is also acknowledged that in the viscous term integration, values of the diffusive fluxes at interfaces between grid nodes are used. Their expressions were obtained from second-order-centered approximations of primary variables [15]. Recently, this numerical method was used to predict mixing regimes in a spatially confined two-dimensional compressible mixing layer [24].

A schematic diagram of the plasma plume expansion is shown in Fig. 1. In order to reduce the total integration time, axisymetric (r, z) modeling is carried out. The axial distance L_z from the substrate is in the range 1.5–3 cm, and the radial one L_r from the symmetry axis is in the range 0.5–2.5 cm. Depending on the computational time to be investigated, L_r and L_z values are chosen to avoid interactions of the plasma plume with the boundaries. The three-dimensional axisymmetric computational domain is meshed with uniform cell size in the r and z direction. Slip-wall conditions are selected at the top. No-slip-wall conditions are imposed on the right and left of the computational cavity. The grid steps used for our calculations are about 20–50 μs. The time step used in our calculations is about 10^{-12} s.

III. RESULTS AND DISCUSSION

A. Initial conditions for hydrodynamic modeling

The initial conditions of the simulation are determined when the laser pulse ends. The initial density, temperature, and velocity profiles are carried out from a one-dimensional (1D) thermal model which accounts for the laser-Si solid target interaction [25]. The 1D model incorporates the inverse bremsstrahlung absorption mechanism for vapor heating through laser-beam-evaporated cloud interaction, the condition of quasineutrality, and the local thermodynamic equilibrium condition for ionization. The Saha equation is used to evaluate ion densities. Typical initial density, temperature, and velocity profiles in the Z direction (cf. Fig. 1), perpendicular to the target surface, are shown in Figs. 2(a)
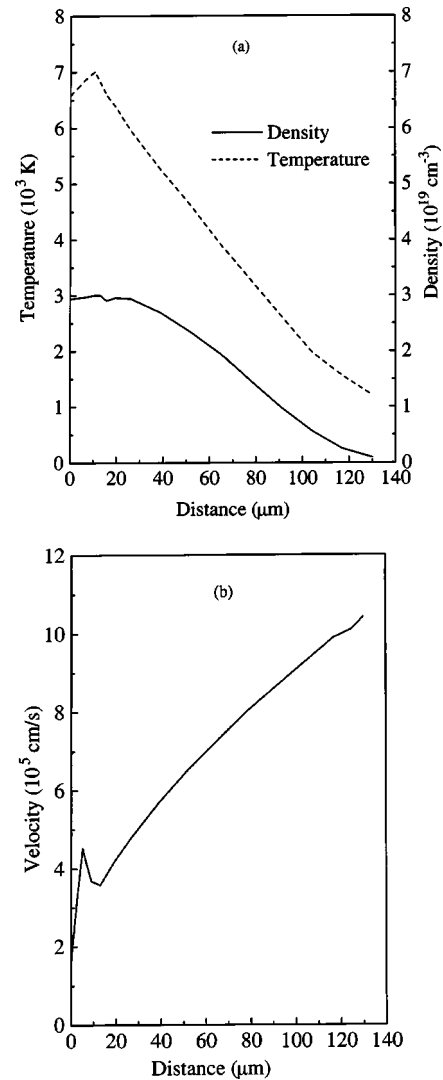
FIG. 2. Initial density (a), temperature (a), and velocity (b) profiles as a function of z position resulting from the 1D thermal modeling calculation at the end of the laser pulse (the FWHM is 15 ns) with a fluence of 1.5 J/cm^2.

and 2(b) for a silicon target irradiated with an ArF laser (λ = 193 nm) with a pulse duration at full width at half maximum (FWHM) of 15 ns and an energy density of. 1.5 J/cm^2. The profiles are given at the end of the laser pulse. At the inner edge of the plasma, the Si density is at a maximum while the velocity is at a minimum. Next the density and the temperature decrease monotonically while the velocity increases linearly. At this laser fluence of 1.5 J/cm^2, slightly above the plasma ignition threshold ($\approx$1.0 J/cm^2) [2,12,13], the maximum ionization degree is about 0.6%. However, at an irradiance of 2.4 J/cm^2, the ionization is $\sim$9%, indicating stronger plasma absorption during the laser pulse.

Thereafter, the background gas surrounding the plasma plume is assumed to be static (i.e., no fluid velocity) and at room temperature 300 K. The background gas (Ar, He) pressure ranges from 100 mTorr to a few Torr.

B. Comparison between Euler and Navier-Stokes computations

We evaluated the effects of diffusion processes on the plume expansion by comparing Navier-Stokes to Euler
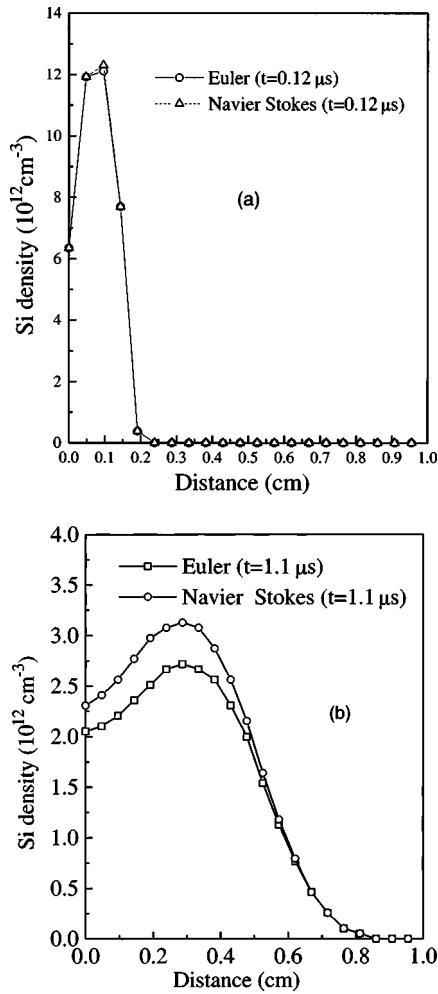
FIG. 3. Comparison of 2D results from Euler and Navier-Stokes gas dynamics calculations, with a laser fluence of 1.5 J/cm^2 and 400 mTorr of Ar: profiles of Si density as a function of Z position and at times $t=0.12\,\mu$s (a) and $t=1.1\,\mu$s (b).

FIG. 4. Results of a 2D Navier-Stokes gas dynamics calculation with a laser fluence of 1.5 J/cm^2 and 400 mTorr of Ar: profiles of temperature (a) and Si density (b) as a function of time at different z positions.

model results. Figures 3(a) and 3(b) show the density profile of Si neutral atoms along the symmetric Z axis at $t=0.12\,\mu$s [Fig. 3(a)] and $t=1.1\,\mu$s [Fig. 3(b)], resulting from the two computations. The modeling conditions were as follows: at a laser fluence of 1.5 J/cm^2, there was 400 mTorr of Ar. At the early expansion stage ($t=0.12\,\mu$s), the Si density profiles provided by the two models are similar. The results show that the convective-mixing regime dominates during the first expansion stage. It may be concluded that a Euler computation which is less complicated than a Navier-Stokes computation can adequately describe the dynamic phenomena, at least during the first expansion stage ($t<200\,$ns), in which the background gas is "snow plowed" and mixed with the leading edge of the plume. At a later expansion stage [$t=1.1\,\mu$s; Fig. 3(b)], the Si density is approximately 10% higher in the Navier-Stokes model for shorter distances ($z<0.4\,$cm), while for longer distances ($z>0.6\,$cm) the densities determined by the two models are quite similar. This indicates that diffusion effects are significant behind the expanding front, and less so in the expanding front ($0.6<z<0.8\,$cm). This is probably due to the fact that the diffusion velocities of Si and Ar atoms are negligible in comparison with the high velocity of the expanding front,

and are significantly increased while the mean velocity of the plume is dramatically decreased behind the expanding front because of the rarefied plume-background-gas interaction. The difference between Euler and Navier-Stokes computations becomes more and more pronounced for longer expansion times. We also found a similar trend with other simulated plume parameters (temperature, velocity). Thus it validates our attempt to use the Navier-Stokes computation to obtain a more accurate description of the plume expansion into background gas. For example, the Navier-Stokes model makes it possible to calculate the diffusion velocities of the different species, which is not the case for the Euler model, where all the species have the same fluid velocity. In the next sections only the results of Navier-Stokes modeling will be presented and discussed.

C. Plume expansion into background gas

Figures 4(a) and 4(b) show the evolution of the density of Si atoms and the temperature at different distances z from the target, respectively. The modeling conditions were as follows: a laser fluence of 1.5 J/cm^2 and 400 mTorr of Ar. At $z=1$ mm, the peak of the Si density (1.3×10^{17} atoms/cm^3) already has a much smaller value (a factor of $\sim$ 250) than
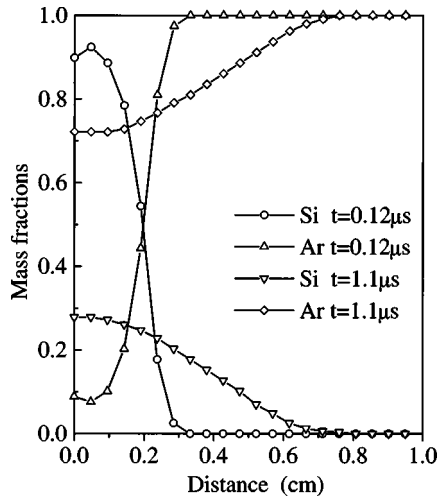
FIG. 5. Results of a 2D Navier-Stokes gas dynamics calculation with a laser fluence of 1.5 J/cm^2 and 400 mTorr of Ar: profiles of mass fraction of Si and Ar as functions of the z position along the symmetry Z axis and at times $t=0.12$ μs (a) and $t=1.1$ μs (b).

that of the maximum density observed at the inner edge of the plasma at $t=0$ (the end of the laser pulse) [see Fig. 2(a)]. Then this maximum of the Si density has both a time and space exponential decrease owing to the very rapid Si plasma expansion. At 0.8 μs and at a distance up to 4 mm, the Si density is quite homogeneous ($\sim 9 \times 10^{15}$ atoms/cm^3), and is now lower than the Ar density of 400 mTorr (1.4 $\times 10^{16}$ atoms/cm^3). The peaks of the temperature (21 000, 17 000, and 8000 K) at distances of 1, 3, and 5 mm, respectively [Fig. 4(b)] are essentially due to the shock heating at the contact front between the Si plasma plume and the Ar gas. Note that at $t=0$ (the end of the laser pulse), the maximum temperature is ~ 7000 K [Fig. 2(b)]. This means that a considerable part of the kinetic energy is converted into internal energy as a result of shock heating. Physically, it is clear that the principal role in the mechanism of shock compression is determined by a viscosity phenomenon rather than by heat conduction [14]. The viscous mechanism causes the scattering of the directed momentum of the plasma plume, and the conversion of the kinetic energy of the forward-directed motion into kinetic energy of random motion, i.e., the conversion of mechanical energy into heat. On the other hand, heat conduction indirectly affects the conversion of mechanical energy because of the redistribution of pressure. As in a cooling process, the exponential diminution of the temperature is in good agreement with experimental observation [12]. For $z=5$ mm and at 0.6 μs, the shock intensity is diminished significantly with a decrease in the maximum temperature of about 8000 K [Fig. 4(b)]. At a longer distance $z=7$ mm the temperature distribution exhibits no peak because of the vanished shock intensity, and the temperature is decrease slowly below 3500 K for $t > 1.2$ μs.

Figures 5(a) and 5(b) show simulated mass fractions of Si and Ar along the symmetric Z axis, at $t=0.12$ and 1.1 μs respectively. The modeling conditions are the same as for Figs. 3 and 4. At the early stage of the plasma expansion ($t=0.12$ μs), Ar gas is mixed with the leading edge of the Si plume at the contact front ($z=0.3$ cm), and the mixing layer
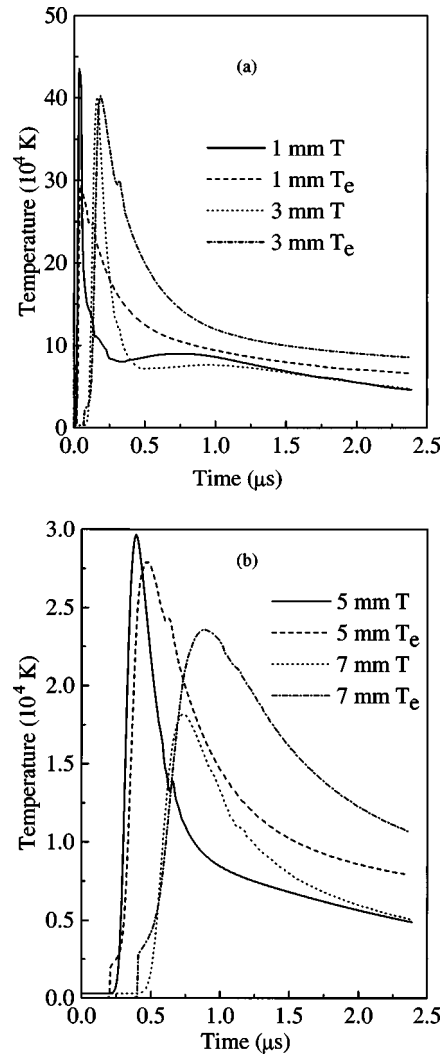
FIG. 6. Results of a 2D Navier-Stokes gas dynamics calculation with a laser fluence of 1.5 J/cm^2 and 400 mTorr of Ar: time evolution of the electrons and heavy-particles temperature at different z positions, 1 and 3 mm (a) and, 5 and 7 mm (b).

is from $z=0.2$ to 0.3 cm. At this early time, some Ar atoms escape from the mixing zone, and begin to move through the Si plasma plume ($z<0.2$ cm). At a later time ($t=1.1$ μs), the mixing zone vanishes, and the Si and Ar gases become a nearly perfect mixture as a result of mass diffusion.

At the beginning of the plasma expansion and close to the surface (initial conditions), the temperatures of electrons and atoms are assumed to be equal as a consequence of local thermodynamic equilibrium conditions during the laser pulse. However, since a two-temperature approach (T and T_e) is used in our modeling because of the nonequilibrium ionization hypothesis, it is interesting to compare their space and time evolution as well as the degree of ionization.

Figures 6(a) and 6(b) show the temporal evolution of the temperature of the electrons and the heavy-particle temperatures at different distances z from the target. The modeling conditions are a laser fluence of 2.4 J/cm^2 and 400 mTorr of Ar. At a distance of 1 mm, the electron temperature is lower than that of the heavy particle in the shock front, which is represented by the peak of the temperature evolution. Between 3 [Fig. 6(a)] and 5 mm [Fig. 6(b)], the electron and
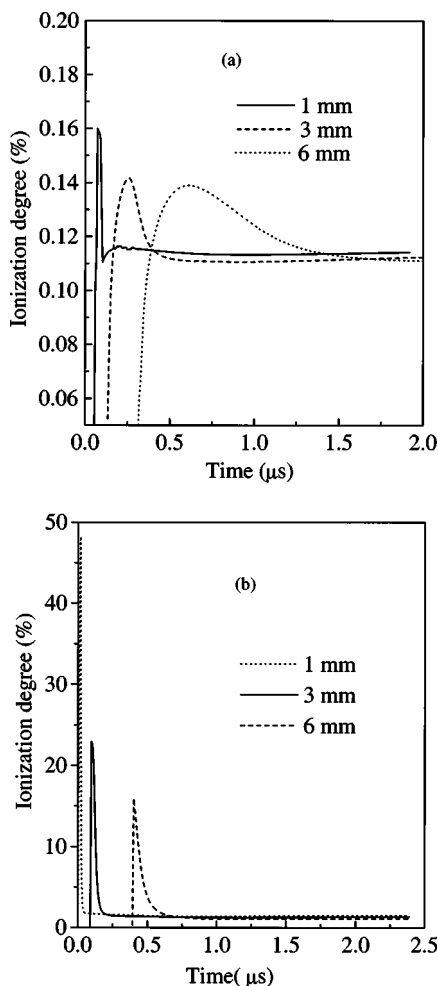
FIG. 7. Initial ionization degree profiles as a function of time and at different z positions resulting from the 1D thermal modeling calculation at the end of the laser pulse (the FWHM is 15 ns) with laser fluences of 1.5 J/cm^2 (a) and 2.4 J/cm^2 (b).

heavy-particle temperatures are approximately equal in the shock front. However, the cooling mechanism is faster for the heavy particles than for the electrons. At a distance of 7 mm from the target surface, T_e is globally higher than T owing to the weakness of the shock front at this location. The differences between the two temperatures at any location are still great at a later time expansion stage ($t > 2\ \mu$s). The slow decrease in electron temperature behind the compression shock compared to that of the heavy particle may be explained by processes such as three body recombination, which dominate when T_e decreases [14].

Figures 7(a) and 7(b) show the degree of ionization as a function of time for different distances from the target, and with 400 mTorr of Ar. For a laser fluence of 1.5 J/cm^2 and at $z = 1$ mm [Fig. 7(a)], the simulated fractional ionization peaks at 0.16%. Like the electron temperature, the ionization degree decreases exponentially with the expansion time as result of the recombination process. For a high laser fluence of 2.4 J/cm^2 and at $z = 2$ mm [Fig. 7(b)], the simulated fractional ionization peaks at ~35% as a result of shock heating (thermal ionization). These ionization peaks appear at the same time as the electron density peaks, and are located in the compressed zone. However, it is noted that the ionization degree falls off dramatically after the shock heating, and it is
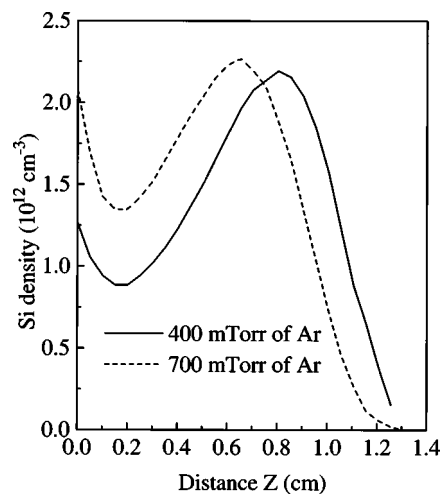
FIG. 8. Results of a 2D Navier-Stokes gas dynamics calculation with a laser fluence of 2.4 J/cm^2 at $t = 2.4\ \mu$s: profiles of the Si density as a function of the z position for Ar pressures of 400 and 700 mTorr.

below 0, 12% and 2.5% at late expansion times for laser fluences of 1.5 and 2.4 J/cm^2, respectively.

D. Influence of background gas pressure and nature

PLD of Si into Ar and He gases has been commonly used to produce Si nanostructures [Eq. (2)]. Thus it is interesting to investigate the influence of the nature and pressure of the background gas on plasma expansion behavior. Figure 8 shows the simulated Si density profile along the symmetry axis Z at $t = 2.4\ \mu$s, and, for a laser fluence of 2.4 J/cm^2, 400 and 700 mTorr of Ar. The increasing Si density near the target surface ($z < 0.2$ cm) with the increasing pressure of Ar indicates that the Si atoms of the rarefied plume are essentially driven by the backward-moving Ar gas as a result of mass diffusion; the backward motion of Si atoms becomes more significant with increasing Ar pressure. The splitting of the Si plume (i.e., two maximum densities) is more pronounced with 700 mTorr of Ar than with 400 mTorr. The numerical results obtained are in good agreement with experimental results, indicating a significant deposition increase of Si particles around the laser spot when the Ar pressure is increased [2].

Figure 9 shows the calculated heavy-particle temperature as a function of time at $z = 5$ mm and for the same conditions as in Fig. 8. The temperature of heavy particles at 700 mTorr is a factor of $\frac{1}{2}$ lower than at 400 mTorr of Ar, as a result of the increasing collision frequency of the Si plume with the cold background gas. A similar trend is also found for He gas.

Figure 10 shows a comparison of the Si density profile along the symmetry axis Z at $t = 1\ \mu$s between a plasma expansion in Ar or He at a pressure of 700 mTorr and a laser fluence of 2.4 J/cm^2. The mean velocity of the Si plume is higher in He than in Ar, and the backward motion of the Si plume is less significant in He than in Ar. Figure 11 shows the temporal distribution of the temperature of heavy particles at $z = 4$ mm. The modeling conditions are the same as in Fig. 10. The temperature with 700 mTorr of Ar is three times as high as with 700 mTorr of He. The difference in the
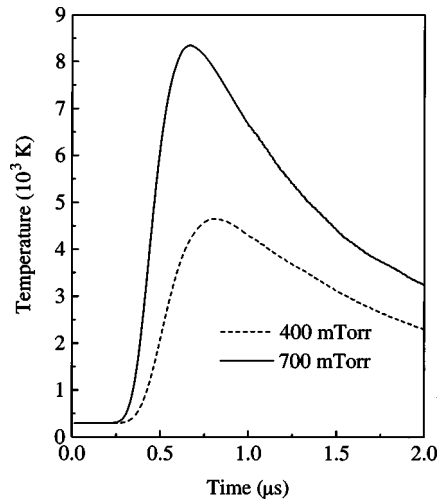
FIG. 9. Results of a 2D Navier-Stokes gas dynamics calculation with a laser fluence of 2.4 J/cm^2 at $z = 5$ mm: profiles of the heavy particle temperature as a function of time for Ar pressures of 400 and 700 mTorr.

temperature and velocity of Si atoms between the Ar and He cases is due essentially to the mass gradient, which significantly affects the conversion of kinetic energy of the Si plume into heat as a result of a compression shock. A quantitative description of the key role of the background gas type and pressure is of great interest to optimize the PLD process.

E. Comparison of modeling to LIF and TOF results

The temporal distribution of the heavy-particle temperature at $z = 1.5$ cm is simulated to be compared to experimental data obtained by the LIF technique [12], as shown in Fig. 12. The modeling conditions are as follows: a laser fluence of 2.4 J/cm^2, and 400 and 1250 mTorr of He. In good agreement with experimental data, the simulated temperature of the atoms decreases exponentially with the expansion time as a result of mixing with the background gas, and the tempera-
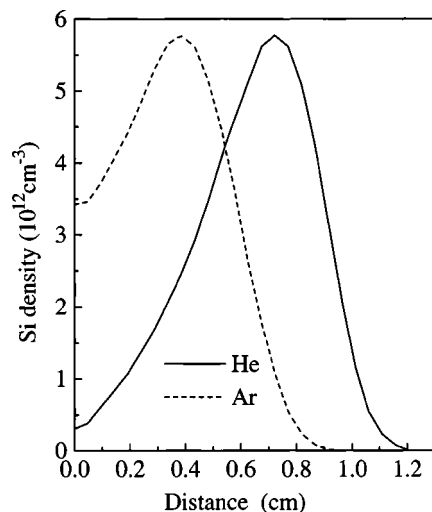
FIG. 10. Results of a 2D Navier-Stokes gas dynamics calculation with a laser fluence of 2.4 J/cm^2 at $t = 1$ μs: Si density profiles as a function of the z position for 700 mTorr of Ar and He.
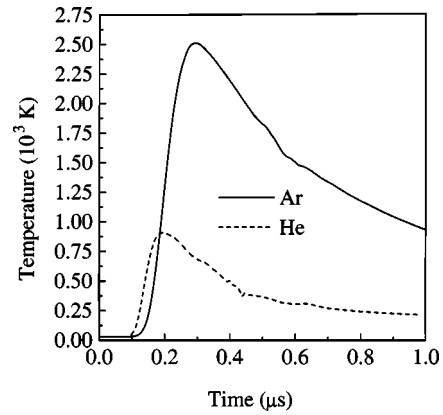
FIG. 11. Results of a 2D Navier-Stokes gas dynamics calculation with a laser fluence of 2.4 J/cm^2 at $z = 5$ mm: Si density profiles as a function of time for 700 mTorr of Ar and He.

ture is significantly below 1000 K for $t > 10$ μs. The spatial and temporal evolution of the temperature and density are of great interest, as these parameters (temperature and density) would be useful to gain a better understanding of the formation of atomic and molecular species.

Figure 13 shows the simulated time of flight (TOF) of Si atoms and ions compared with experimental data, which were obtained with a laser fluence of 2.4 J/cm^2 and for 400 mTorr of Ar. For shorter distances (<5 mm), the simulated time of flight of Si neutral atoms is in good agreement with experimental data. The discrepancies between calculations and experimental data become more pronounced at longer distances (>6 mm). This is probably due to chemical processes such as clustering which may occur more significantly in the last expansion stage. An important question is whether the ambipolar diffusion concept (i.e., forced diffusion) considered in the model can adequately describe the experimental observation of ion acceleration in the last expansion stage. Experimentally, it is observed that the ion expansion velocity is twice as fast as that of the neutral atom, as shown in Fig. 13. The simulated ion velocity is only 5% faster than the simulated atom velocity as a result of ambipolar diffu-
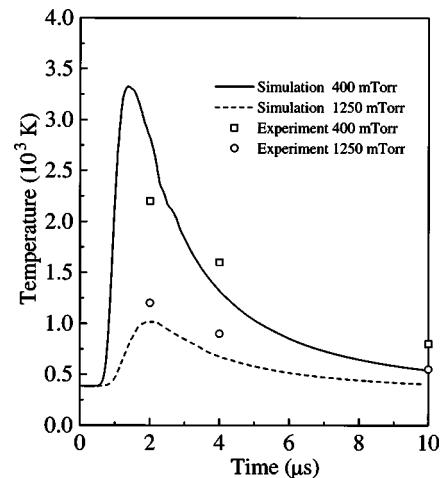
FIG. 12. Comparison of calculated and experimental profiles obtained by the LIF technique of heavy particle temperature at $z = 1.5$ cm as a function of time, for a laser fluence of 2.4 J/cm^2, and background pressures of 400 and 1250 mTorr of He.
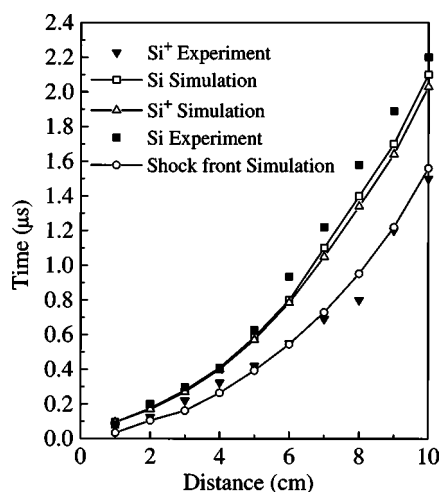
FIG. 13. Comparison of calculated and experimental time-of-flight (TOF) data of Si atoms and ions for a laser fluence of 2.4 J/cm^2, and a background pressure of 400 mTorr of Ar.

sion. The simulated values of the ion TOF are far from being satisfactory. We also note from our modeling study that for a laser fluence of 1.5 J/cm^2, slightly above the silicon plasma ignition threshold (1 J/cm^2), the lack of agreement still exists. So the ambipolar diffusion concept cannot adequately describe the ion dynamics because of the possible small degree of charge separation in the plume. Thus charge separation phenomena may be very strong in the plasma plume, and have to be treated rigorously in the numerical model. In addition, the shock front expansion is also compared with the dynamics of the species (see Fig. 13). The shock front velocity is approximately twice as fast as the neutral atom velocity. Thus the majority of neutral atoms move far behind the shock wave.

The velocity of the shock front (simulated) and of the ions (TOF measurements) indicates that ion dynamics are strongly correlated with the shock front expansion. An explanation of this behavior may be that fast electrons accelerate ions behind the shock front.

IV. SUMMARY AND CONCLUSION

The details of physical phenomena involving laser-induced Si plasma expansion into Ar and He gases is considered after the end of a laser pulse of an excimer laser (an ArF of 193 nm) at a fluence range of 1.5–2.4 J/cm^2. This is high enough to provide a good supply of singly ionized Si, while avoiding higher ionization states. The background pressure is investigated in the range of a few hundred mTorr. A hydrodynamic multispecies gas model simulating the involved processes is proposed. The plasma and background

gas are treated as a compressible fluid. The hydrodynamic model is set up with four species (Si I, Si II, Ar I, and e). The model incorporates the nonequilibrium condition for ionization and, for the first time, to our knowledge, various diffusion processes (mass and ambipolar diffusion, thermal conduction, and viscosity). We use a two-temperature approximation (heavy-particle temperature, electron temperature) to describe the plasma. The ambipolar diffusion concept is tested to describe the effect of forced diffusion by the electric field, which is assumed to cause the ion acceleration process in the plasma expansion. We solve the three-dimensional axisymmetric compressible Navier-Stokes equations for a multispecies gas with thermal conduction, mass, forced diffusion, and viscosity in addition to convection.

The effects of diffusion processes are evaluated by comparing the solutions of the full set of Navier-Stokes equations that contain convection, thermal conduction, viscosity, mass, and forced diffusion to the Euler solutions obtained by solving only the convection. It is demonstrated that diffusion processes are only important in the last expansion stage, and are less significant in the first stage. Therefore, a Euler computation which is less complicated than a Navier-Stokes computation can adequately describe the early stage of plasma expansion into background gas. Despite a number of simplifications in the model, it is possible to simulate adequately the overall plasma expansion behavior—such as the mixing zone evolution, the temperature, and the density evolution of the plasma plume—into the background gas. The rarefied plasma plume—background gas interaction leads to a backward movement including both the plume species and background gas as a result of mass diffusion. There is a marked difference between heavy-particle and electron temperatures, indicating a persistent lack of equilibrium between the heavy particle and the electron in the plasma plume expansion. The numerical results are applied successfully to Si neutral atom dynamics. However, our attempt to use the ambipolar diffusion concept to describe the ion dynamics was unsuccessful, since the calculated ion velocity is slightly greater (5%) than the neutral atom velocity, whereas the experimental ion velocity is twice as fast as the neutral atom value. Thus charge separation phenomena may be very strong in the plasma plume, and have to be treated rigorously in the numerical model. We also outline the strong correlation of the shock front expansion with ion dynamics. A quantitative prediction of the critical influence of the background gas type (Ar, He) and pressure is demonstrated. Thus it is quite possible to control ''the plasma plume expansion'' by only varying the background gas parameters (pressure, type). The extension of the applicability of the model to the case of Si dimer formation in the gas phase is also underway, to gain a better understanding of the clustering process.

[1] *Pulsed Laser Deposition of Thin Films*, edited by D. B. Chrisey and G. K. Hubler (Wiley, New York, 1994).

[2] I. A. Movtchan, W. Marine, R. W. Dreyfus, H. C. Le, M. Sentis, and M. Autric, Appl. Surf. Sci. **96-98**, 251 (1996).

[3] R. K. Singh and J. Narayan, Phys. Rev. B **41**, 8843 (1990).

[4] S. I. Anisimov, D. Bäuerle, and B. Luk'yanchuck, Phys. Rev.

B **48**, 12 076 (1993).

[5] A. Vertes, R. W. Dreyfus, and D. E. Platt, IBM J. Res. Dev. **38**, 1 (1994).

[6] R. F. Wood, K. R. Chen, J. N. Leboeuf, A. A. Puretzky, and D. B. Geohegan, Phys. Rev. Lett. **79**, 1571 (1997).

[7] J. N. Leboeuf, K. R. Chen, J. M. Donato, D. B. Geohegan, C.

L. Liu, A. A. Puretzky, and R. F. Wood, Appl. Surf. Sci. **96-98**, 14 (1996).

[8] T. E. Itina, A. A. Katassonov, W. Marine, and M. Autric, J. Appl. Phys. **83**, 6050 (1998).

[9] A. V. Bulgakov and N. M. Bulgakova, J. Phys. D **28**, 1710 (1995).

[10] H. C. Le, J. Vuillon, D. Zeitoun, W. Marine, M. Sentis, and R. W. Dreyfus, Appl. Surf. Sci. **76**, 96 (1996).

[11] P. E. Dyer, R. D. Greenough, A. Issa, and P. H. Key, Appl. Phys. Lett. **53**, 534 (1988).

[12] H. C. Le, R. W. Dreyfus, W. Marine, M. Sentis, and I. A. Movtchan, Appl. Surf. Sci. **164**, 96 (1996).

[13] G. B. Shinn, F. Steigerwald, H. Stiegler, R. Sauerbrey, F. K. Tittel, and W. L. Wilson, J. Vac. Sci. Technol. B **4**, 1273 (1986).

[14] Ya. B. Zel'dovich and Yu. P. Raizer, *Physics of Shock Waves and High Temperature Phenomena* (Academic, New York, 1966).

[15] E. Oran and J. P. Boris, *Numerical Simulation of Reactive Flow* (Elsevier, New York, 1987).

[16] C. F. Curtiss and J. O. Hirschfelder, J. Chem. Phys. **17**, 550 (1949).

[17] J. Lee, AIAA J. **84**, 1729 (1984).

[18] E. A. Mason and S. C. Saxena, Phys. Fluids **1**, 631 (1958).

[19] C. R. Wilke, J. Chem. Phys. **18**, 517 (1950).

[20] R. J. Kee, G. Dixon-Lewis, J. Warnatz, M. E. Coltrin, and J. A. Miller (unpublished).

[21] T. E. Morse, Phys. Fluids **6**, 1420 (1963).

[22] J. P. Boris, F. F. Grinstein, E. S. Oran, and R. L. Kolbe, J. Fluid Dynamic Res. **10**, 199 (1992).

[23] E. Oran and J. P. Boris, *Numerical Simulation of Reactive Flow*, 235 (Elsevier, New York, 1987).

[24] P. Vuillermoz and E. S. Oran, Proc. R. Soc. London, Ser. A **449**, 351 (1995).

[25] J. C. Gauthier, J. P. Geindre, N. Grandjouan, and J. Vivamont, J. Phys. D **15**, 32 (1983).